The Cryosphere, 20, 2723–2734, 2026
https://doi.org/10.5194/tc-20-2723-2026


The Cryosphere Open Access EGU

# Impact of surface melt and brine infiltration on fracture toughness of ice shelves

**Emma Pearce[1], Oliver J. Marsh[1], Thomas M. Mitchell[2], Jukka Tuhkuri[3], Elizabeth R. Thomas[1], and Siobhan Johnson[4,1]**

[1]British Antarctic Survey, Cambridge, United Kingdom
[2]Rock and Ice Physics Laboratory, University College London, London, United Kingdom
[3]Aalto University, Espoo, Finland
[4]Yusuf Hamied Department of Chemistry, University of Cambridge, Cambridge, United Kingdom

**Correspondence:** Emma Pearce (emmear@bas.ac.uk)

Received: 3 October 2025 – Discussion started: 5 November 2025
Revised: 27 March 2026 – Accepted: 11 April 2026 – Published: 12 May 2026

**Abstract.** Ice shelves are heterogeneous composites of firn, meteoric ice, refrozen melt and brine-saturated ice. The properties and distribution of these elements control ice shelf response to stress and susceptibility to fracturing. Here, we quantify how surface-melt and brine infiltration modify the Mode I fracture toughness ($K_{Ic}$) of meteoric ice on the Brunt Ice Shelf (BIS), Antarctica. During the 2023/2024 austral summer, we recovered a 37 m core sequence from meteoric infill ice near Halley VI, where radar mapping shows continuous brine horizons at $\sim$ 37 m depth and line scans indicate that the upper 37 m contain $\sim$ 7 % refrozen melt. We combined density, salinity, temperature and grain size measurements with semi-circular three-point bending tests on samples representing (i) meteoric ice, (ii) melt-modified meteoric ice, and (iii) brine-infiltrated meteoric ice. Our results show melt-modified samples are consistently tougher than melt-free meteoric ice, with $K_{Ic}$ increases up to $\sim$ 40 %. This is despite their larger grain size, indicating densification dominates over grain-size effects. In contrast, brine-saturated meteoric ice exhibits markedly lower $K_{Ic}$, by 14 %–34 % relative to density-matched, brine-free meteoric ice, consistent with chemical weakening and lower freezing temperatures. Our results demonstrate that as $K_{Ic}$ varies strongly with density, salinity and depth, a spatially and temporally constant toughness value is unlikely to reproduce calving behaviour accurately. Implementing spatially and vertically variable $K_{Ic}$ values, and understanding how ice shelf structure and composition evolves over time, is essential to improve predictions of rift propagation and calving.

## 1 Introduction

Antarctic ice shelves play an essential role in restraining the flow of inland glacier ice. They can be weakened by basal-melt – driven thinning (Pritchard et al., 2012) or surface-melt – induced hydrofracture leading to acceleration in the flow of grounded glacier ice (Scambos et al., 2004), and increasing the contribution to global sea level rise. The rapid collapse of the Larsen B Ice Shelf in 2002 serves as an example of this process, where following the disintegration of the ice shelf, inland ice velocities quadrupled (Glasser and Scambos, 2008; Scambos et al., 2004).

Part of the natural cycle of ice shelf growth and deterioration in stable conditions is ice shelf rifting, where full-thickness fractures create tabular icebergs (De Rydt et al., 2019). Rifts nucleate from pre-existing weaknesses in the ice shelf, caused by the build-up of stress around pinning points or shear margins (Larour et al., 2004; Walker et al., 2013; Bassis et al., 2005; Fricker et al., 2005a). Rift growth is episodic, with bursts of propagation occurring over hours to days and often accompanied by rapid widening and an increase in seismic activity (Fricker et al., 2005b, a). While rift paths broadly follow the principal extensional stress field set by the ice shelf geometry and flow direction (Larour et al., 2004; Walker et al., 2013), their timing and rate depend on both external forcing and local material properties (Borstad et al., 2017; Kulessa et al., 2019; Lipovsky, 2020).

To add complication to the rifting process, ice shelves are not made up of homogeneous ice; they are complex

composites of firn, refrozen melt, meteoric ice, and marine ice, with mechanical properties that vary both spatially and with depth. Processes such as surface melting can introduce centimetre-scale melt layers that span hundreds of metres horizontally, increasing the density of the upper surface and reducing porosity. In extreme melt conditions, such as those caused by the high summer temperatures on the Larsen C Ice Shelf, melt ponding, and refreezing can introduce ice slabs up to 60 m thick within the firn (Hubbard et al., 2016). Brine infiltration adds further inhomogeneity and can, in particular, alter the mechanical character of ice, as saline porewater reduces freezing temperature, enhances ductile failure, and promotes chemical weakening at grain boundaries (Cruz and Lipovsky, 2025). Marine suture zones, where brine and refrozen seawater are incorporated into the ice shelf, have been shown to be pervasive around the continent (Cook et al., 2018) and to both arrest rift propagation in some settings and enhance fracture in others, underscoring the highly variable role of brine in rift propagation (e.g., Kulessa et al., 2019; Borstad et al., 2017; Killingbeck et al., 2025).

In ice-fracture modelling, it is assumed that most rifts on ice shelves grow predominantly in Mode I (opening) under tensile or flexural-tensile stresses, and hence can be represented in two ways. Firstly by linear-elastic fracture mechanics, which treats rifts as cracks in a thin, elastic plate loaded by along-flow tension and by flexure from tides and waves, where propagation is dictated by the condition that the Mode I stress-intensity factor must exceed the local fracture toughness ($K_I \geq K_{Ic}$) (e.g., van der Veen, 1998; Lipovsky, 2020; Clayton et al., 2024). Secondly, by continuum-damage models that present rifting using an internal damage field that concentrates damage into rifts and reproduces observed spatial patterns of weakening. These approaches have been used to assess rift stability at the shelf-wide scale (e.g., Borstad et al., 2017, 2012; Krug et al., 2014; Huth et al., 2023).

Across both types of models, the key material parameter controlling the advance of the fracture is the Mode I fracture toughness, $K_{Ic}$ (in the order of $100\,\mathrm{kPa\,m^{0.5}}$ for glacier/shelf ice), which sets the threshold for crack growth and therefore controls predicted rift initiation and the timing of calving (Rist et al., 2002; Lipovsky, 2018). Rift growth is a threshold process, excluding subcritical growth (Weiss, 2004; Atkinson, 1984), and as such, propagation can only occur once the stress intensity factor exceeds the maximum local $K_{Ic}$ along the fracture path. This implies that rifts must accumulate sufficient elastic energy to overcome zones of high fracture toughness before they can advance, which explains their episodic growth behaviour (Van der Veen, 1998).

Laboratory and field measurements show that the fracture toughness of glacier ice ($K_{Ic}$) spans a wide but poorly constrained range, depending on microstructure and physical state, where fracture toughness has been shown to depend on temperature, density, grain structure, and environmental conditions (Schulson, 2001; Schulson and Duval, 2009; Rist et al., 2002). Classic laboratory tests on freshwater polycrystalline ice established the baseline mechanics where $K_{Ic}$ typically lies between $100–300\,\mathrm{kPa\,m^{0.5}}$ at below zero temperatures, but decreases rapidly toward the melting point, where ice with values of $\sim 300\,\mathrm{kPa\,m^{0.5}}$ at $-10\,^{\circ}\mathrm{C}$ can fall to $\sim 200\,\mathrm{kPa\,m^{0.5}}$ near $-5\,^{\circ}\mathrm{C}$ (Schulson, 2001; Rist et al., 2002; Dempsey, 1991).

Grain size exerts a strong control, with larger grains lowering toughness by facilitating inter-granular fracture, while finer grains inhibit crack advance and promote higher $K_{Ic}$(Nixon and Schulson, 1987; Rist et al., 2002), with $K_{Ic}$ decreasing from $\sim 300\,\mathrm{kPa\,m^{0.5}}$ at grain sizes of $\sim 1\,\mathrm{mm}$ to $\sim 150\,\mathrm{kPa\,m^{0.5}}$ at grain sizes of $5-10\,\mathrm{mm}$ (Nixon and Schulson, 1987). Density and porosity further control toughness, where shallow, porous firn can be as low as $50–100\,\mathrm{kPa\,m^{0.5}}$, compared to compact meteoric ice at depth, which can exceed $300\,\mathrm{kPa\,m^{0.5}}$ (Rist et al., 2002; Alley and Bentley, 1988). Previous work by Rist et al. (1996, 2002) provided a foundational understanding of how fracture toughness varies with depth and microstructure in an Antarctic ice shelf. Using three-point bend and uniaxial compression testing on ice cores from the Ronne Ice Shelf, they found that apparent fracture toughness increases steadily through the firn and meteoric ice layers before plateauing in denser ice. Their results demonstrated a strong positive correlation between $K_{Ic}$ and density, with little to no dependence on grain size once a sufficient number of grains were present across the specimen diameter. They also observed that brine-influenced ice tends to exhibit lower and more variable toughness, potentially due to chemical weakening or inter-granular flaws.

Most existing measurements of $K_{Ic}$ for glacier ice have been derived from clean, cold, meteoric ice, leaving uncertainty for melt-affected or brine-infiltrated marine ice. Limited studies on chemical effects have been shown to lower $K_{Ic}$, as solutes concentrate along grain boundaries and promote semi-liquid, inter-granular films that weaken cohesion (Cullen and Baker, 2001). Furthermore, laboratory tests on saline sea-ice similarly demonstrate that fracture toughness decreases with increasing brine volume, with the associated reduction in freezing temperature driving additional weakening (Timco and Frederking, 1983).

Ice-shelf calving models often utilise idealised, constant toughness values across the whole ice shelf in the range of $100-200\,\mathrm{kPa\,m^{0.5}}$ for brittle fracture thresholds (e.g., Pralong and Funk, 2005; Albrecht and Levermann, 2012; Borstad et al., 2012; Krug et al., 2014; Christmann et al., 2015), despite evidence that natural variability is far larger and that differences in ice shelf composition can strongly influence ice shelf dynamics (e.g., Craw et al., 2023). Furthermore, as Antarctica warms, ice shelves are projected to thin (Naughten et al., 2023), snow accumulation rates increase (Nicola et al., 2023), and melt events become more common (Orr et al., 2023), hence ice shelves will develop increasingly heterogeneous structures dominated by firn, melt and brine infiltration.

Since the 1990s, many ice shelves have thinned by tens of metres due to enhanced basal melting (Pritchard et al., 2012; Adusumilli et al., 2020; Naughten et al., 2023), while episodic surface melt events and ponding have intensified in regions of the Antarctic Peninsula and West Antarctica (Scambos et al., 2009; Wille et al., 2022). Crack initiation and propagation thresholds on ice shelves should be expected to be neither spatially uniform nor constant through time, and will consist of an array of toughness values controlled by grain size, density, temperature, porosity, and impurity content.

In this study, we directly quantify how re-frozen surface–melt and brine infiltration modify the Mode I fracture toughness ($K_{Ic}$) of ice from the Brunt Ice Shelf (BIS). We extend previous laboratory results (e.g., Rist et al., 1996, 2002) by directly contrasting refrozen melt with brine infiltration in meteoric ice of similar density. This isolates the competing effects of melt-driven densification versus brine-induced weakening, providing the first controlled dataset to quantify both processes in Antarctic shelf ice.

## 2 Brunt Ice Shelf

The Brunt Ice Shelf (BIS) is situated along the Eastern coast of the Weddell Sea, flowing north-west from the Caird Coast of Coats Land. It forms the southernmost section of a complex ice shelf system made up of the Stancomb-Wills Glacier Tongue and the Riiser-Larsen Ice Shelf to the east (Fig. 1).

The BIS exhibits a heterogeneous structure resulting from its unique formation processes. As ice flows off the continent over a steep grounding zone, it undergoes extensive crevassing, leading to the fragmentation of the ice into large blocks measuring between 2500 and 6000 m in length and 250–900 m in width (King et al., 2018). These blocks, composed primarily of dense continental ice, are interspersed with zones of sea ice, creating a mosaic-like structure. Accumulated snowfall and drifted snow fills the surface depressions between the blocks, smoothing the surface topography. Ground Penetrating Radar (GPR) data have found the thickness of the ice shelf to vary between the thick (approximately 250 m) continental ice blocks interspersed with the thinner (approximately 150 m) sections of sea and meteoric infilled ice (King et al., 2018). Hereafter we refer to the mix of infilled compressed snow and sea ice as "infilled" ice.

Due to the porous and permeable nature of the infilled ice sections, seawater (brine) can propagate through these areas and reach the height of sea level (approximately 30–40 m below the surface), leading to brine-saturated ice below this level. The brine infiltrates when isostatic loading by snow accumulation on the sea ice layers pushes the sea ice below sea level. Since the firn has not fully consolidated to pore close-off, it is still porous and permeable, allowing seawater to infiltrate. Radar mapping shows that the BIS has these continuous brine layers within the infilled ice, disappearing in the more dense, impermeable continental ice blocks (King et al., 2018) (Fig. 1). Analogous surveys on the McMurdo and Larsen C Ice Shelves confirm the same radar signature of brine (Grima et al., 2016; Killingbeck et al., 2025).

Over the past five years, two major rift systems, Chasm 1 and Halloween Crack, have developed on the BIS, culminating in the calving of two large tabular icebergs: A-81 in January 2023 and A-83 in February 2024. Following the calving of iceberg A-81, the ice shelf's flow speed increased from an average of 1–2.5 m d$^{-1}$ to approximately 4 m d$^{-1}$, attributed to the loss of buttressing provided by the McDonald Ice Rumples (Marsh et al., 2024). As both these rifts progressed, they preferentially followed the zones of infill ice, while frequently slowing or arresting at the denser blocks of continental ice.

The interplay between the BIS's structural composition and rift dynamics underscores the importance of understanding the mechanical properties of its constituent ice types. Investigating how features like melt layers and brine infiltration affect fracture toughness is crucial for improving predictive models of ice shelf stability and potential contributions to sea-level rise.

## 3 Data and Methods

During the 2023/2024 Antarctic summer season, an ice core was recovered from a 37 m borehole drilled close to the site of Halley VI research station (Fig. 1). Data were collected from the infilled ice (site S2), to establish variations in ice properties and the controls these have on fracture toughness of the "weaker" ice type. Site S2 was located using GPR data to ensure the core was collected from an area where brine infiltration was present. The approximate thickness of the ice at this location is 150 m, established from freeboard calculations and density measurements.

### 3.1 Ice core recovery and borehole measurements

A medium-depth mechanical ice core drill (Mulvaney et al., 2002) was used to recover a continuous ice core record of 37 m, made up of 44 segments, numbered sequentially by recovery order. We use this number to identify segments in the text (e.g. segment 35). Each segment was approximately 105 mm in diameter, with lengths up to 90 cm, although segment length varied during drilling. Drilling was stopped at 37 m depth after two days when brine infiltration saturated the ice and prevented further drilling progress.

As core segments were recovered, they were measured and weighed to obtain an average density with depth. Once drilling was finished, seven TinyTag temperature loggers were placed at 2.5 m intervals down the borehole and left overnight (Fig. 2). The loggers were then raised by 2 m and left for a further 3 h to obtain additional temperature measurements.

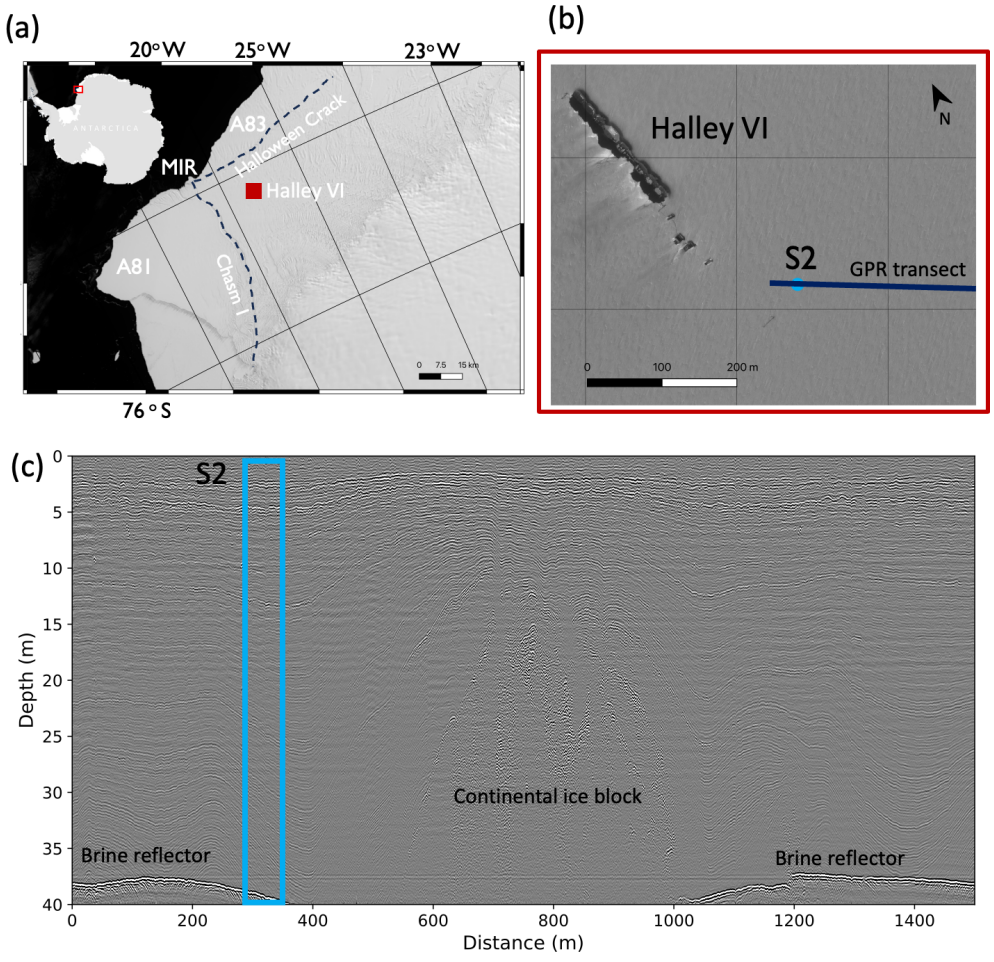


**Figure 1.** **(a)** The location of the Brunt Ice Shelf in East Antarctica and the McDonald Ice Rumples (MIR), which acts as a grounded pinning point for the ice shelf. **(b)** A close-up of the red box in figure **(a)** showing the British Antarctic Survey's Halley VI research station, the location of the drill site, S2, next to the station, and the location of the GPR transect line shown in figure **(c)**. GPR data acquired to locate a block of continental ice and the infilled ice. Brine infiltrates to a depth of approximately 37 m in the permeable infilled ice. Isochrones in the GPR data highlight annual layering, with brighter reflections linked to visible melt layers observed in the core.

The core segments were returned to the UK by the RRS Sir David Attenborough, being kept at a constant temperature of −20 °C. The segments were then stored at the British Antarctic Survey's ice core facility, remaining at −20 °C.

### 3.2 Line Scan

The core was pre-processed by cutting the segments in half lengthwise. One-half of each segment was line-scanned to enable the identification of melt. Melt thickness was calculated by measuring the depth of the top and bottom of a continuous melt layer. The total melt within the 37 m of collected core equated to 2.47 m, 6.68 % (Fig. 2b).

### 3.3 Thin Sections

Two vertical thin sections were prepared from segment 35 (29 m depth) to assess the ice crystal structure and grain size of the meteoric infilled ice and the melt inclusions. The thin sections were levelled with a band saw and mounted onto glass plates using water at 0 °C, then thinned with a microtome to a thickness less than one grain-size. The sections were examined on a light box under cross-polarised light to determine grain size and crystal structure (Fig. 3). Both sections were visually identified as exhibiting isotropic crystal fabrics. The section without visible melt features had an average grain size of 1 mm, whereas the melt-affected section displayed larger grains (5–10 mm).

### 3.4 Salinity measurements

Measurements were obtained from discrete ice samples cut from segments 41, 42, 43 and 44. Samples cut for salinity determination were melted in sealed glass jars and the meltwater was analysed using a SciQuip Precision SQ-7071 conductivity and temperature meter. This instrument has a reported

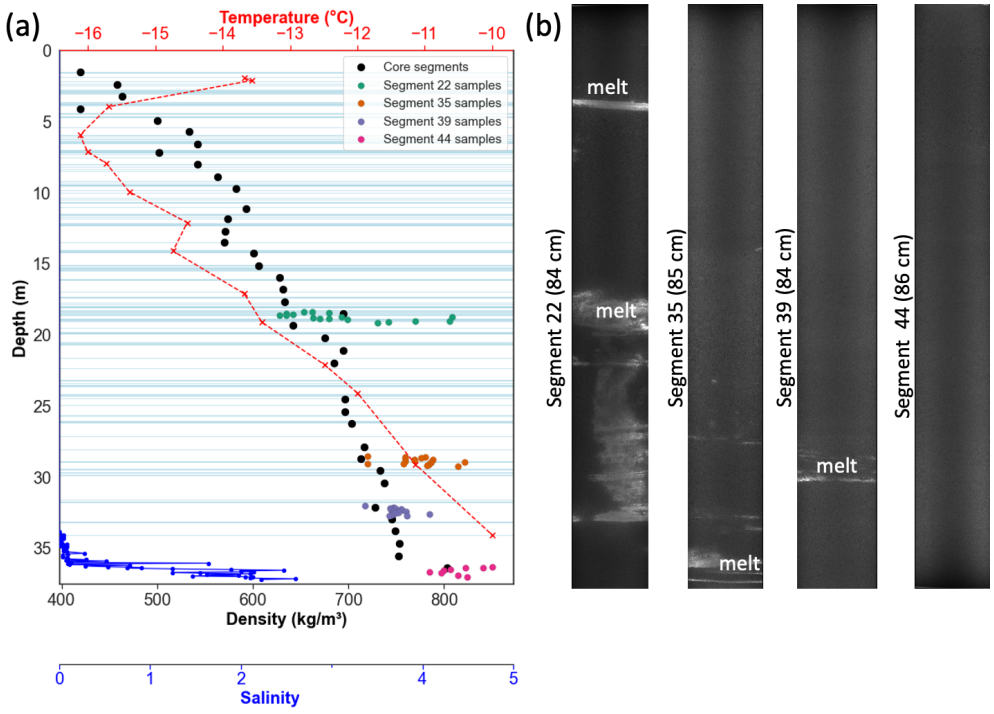


**Figure 2. (a)** Density measurements for whole segments (black) measured in the field, and smaller samples cut from the same segments used for fracture analysis (green, orange, purple, pink) measured in the lab. The spread in density of the smaller samples is due to some samples containing refrozen melt, which increases those samples' density relative to the average segment density. Refrozen melt layers within the core are shown by the background blue bands. Red dashed line shows temperature data recorded at specific depth intervals using TinyTag loggers. **(b)** Line-scanned segments for segment 22 (with a top depth of 16.45 m), segment 35 (27.67 m), segment 39 (31.07 m) and segment 44 (35.92 m). Line scan data highlight the melt within the segments.

accuracy of 0.5 % of its maximum measurement range for conductivity and 0.5 °C for temperature. The practical salinity (PSS-78) of the samples was calculated using the relationship between pressure, temperature and conductivity as outlined in Lewis (1980).

The salinity of the Weddell Sea is approximately 35 ‰ (Foster and Carmack, 1976). Our values (Fig. 2a), show an average salinity of between 0.2 ‰ and 0.8 ‰ for samples above 35 m, reaching a maximum salinity of 2.2 ‰ at the bottom of the borehole, at approximately 37 m depth.

### 3.5 Ice Fracture Samples

Four segments were selected to run fracture analysis tests on: segment 22 (with a top depth of 16.45 m), segment 35 (27.67 m), segment 39 (31.07 m) and segment 44 (35.92 m). The segments were chosen due to their differing densities, melt inclusion and the presence of brine saturation (segment 44), enabling a wide span of fracture toughness measurements to be obtained. Each segment produced between 9–17 samples, by following the method of Kuruppu et al. (2014), numbered from 1 to $N$, with 1 representing the shallowest sample cut from each segment. Semi-circular samples were prepared for use with a three-point bending test to determine the Mode I static fracture toughness of the ice (Fig. 4).

**Table 1.** Dimensions of the SCB sample. The dimensions were selected based on the work by Kuruppu et al. (2014).

| Variable | Criteria | Size (mm) |
|---|---|---|
| $T$ | $T \geq 0.4D$ | 42 |
| $D$ | $D \geq 10\times$ grain size | 105 |
| $a$ | $0.4 \leq a/R \leq 0.6$ | 26 |
| $S$ | $0.5 \leq S/D \leq 0.8$ | 80 |

The sample's diameter is related to the average grain size in the ice by a ratio of at least 10 : 1, and the minimum sample thickness is the larger of 0.4D or 50 mm (Table 1).

The samples were stored and prepared at −15 °C using a band saw to cut the semi-circles perpendicular to the segment long axis. Once the samples were of the correct thickness and diameter, they were weighed to get an accurate sample density (Fig. 2). A notch was then cut into the samples using a thin cutting blade. Before fracturing, the notch tip was scored with a very thin blade to ensure the notch tip was less than the average grain size of the sample. The thickness ($T$) and radius ($R$) of each sample were measured four times to the

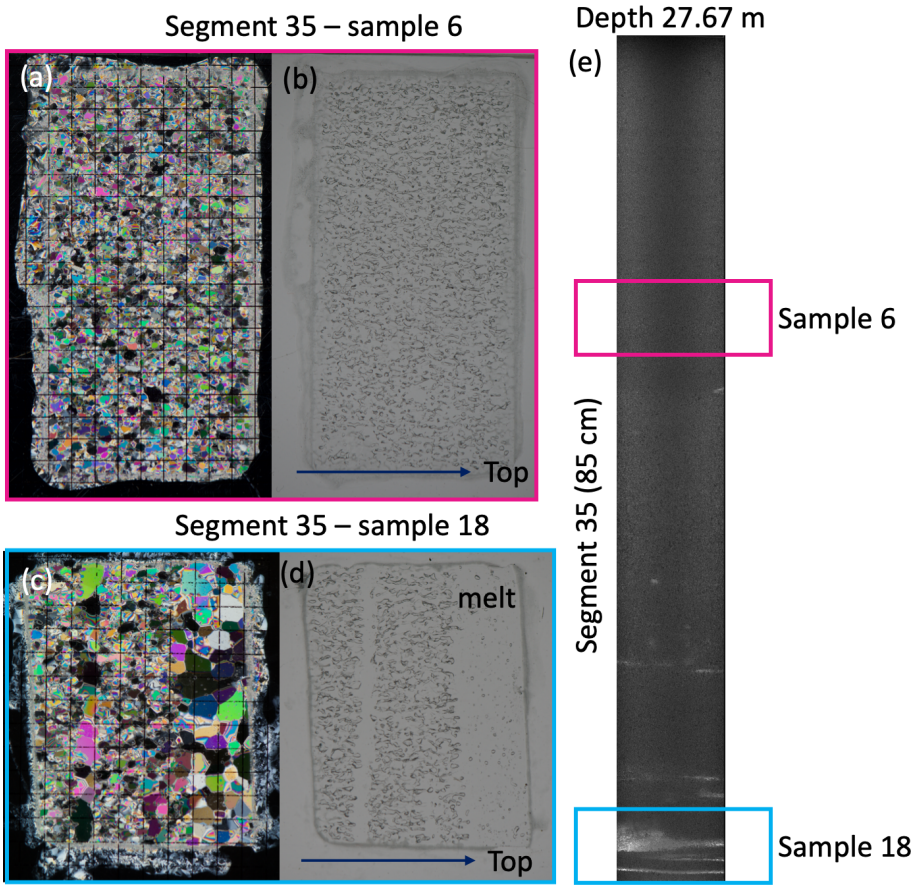


**Figure 3.** **(a)** a 5 mm grid overlaid on a thin section under polarised light taken from segment 35, sample 6 of meteoric, infilled ice with no melt present. **(b)** The thin section sample with no polarised light. **(c)** Thin section taken from sample 18 of the same segment, with the presence of a melt layer shown under polarised light. The melt layer exhibits larger grain size and fewer bubbles than the surrounding ice. **(d)** The thin section with the melt is shown under normal light. **(e)** Segment 35 from which the thin sections are taken.

closest millimetre. The notch length ($a$) was also measured four times after the samples were fractured, to ensure as accurate a reading as possible. If the sample had the presence of melt (visible by eye), the surface area of melt on the fractured surface was measured post-breaking of the sample, and a melt percentage was given for that sample.

The fracture tests were performed using a compressive hydraulic test system with the facilities to record the load and axial displacement. The load application is performed via a conventional three-point bend fixture, with the sample placed on two cylindrical rollers. The sample is then loaded at a constant displacement rate of 0.01 mm $s^{-1}$, with the displacement and the load recorded at 200 Hz. Our experimental approach includes refined fracture testing using a semi-circular bend specimen (SCB). This setup is particularly sensitive to differences in fracture behaviour in low-density samples such as firn, enabling more precise measurement of crack initiation and propagation, and offers tighter control over notch geometry and crack length than the three-point bending tests previously used on Antarctic shelf ice (e.g., Rist et al., 1996). This makes it especially effective for detecting toughness contrasts introduced by melt inclusions or brine. All samples were stored and prepared at −15 °C. Experiments were conducted in a room where temperatures fluctuated between −10 and −15 °C at the University College London cold room facilities, with experiment times ranging between one to three minutes, depending on the sample.

## 4 Results: Fracture Toughness

Following the work of Kuruppu et al. (2014), mode I fracture toughness ($K_{Ic}$) of a sample, of thickness $T$ can be calculated using the peak force ($P_{max}$) (Fig. 5) as,

$$K_{Ic} = Y' \frac{P_{max}\sqrt{\pi a}}{2RT} \quad (1)$$

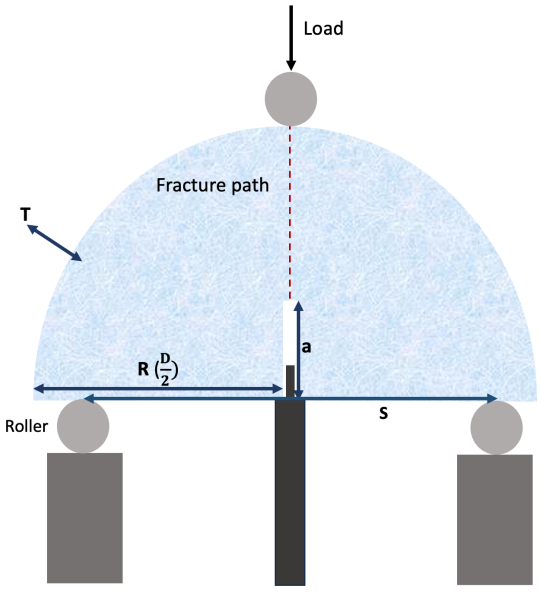


**Figure 4.** Experiment set up for ice fracture tests with semi-circular bend samples. $T$ refers to sample thickness, $R$, sample radius, $S$, the separation between rollers, and $a$, the notch length. Specimens were loaded via cylindrical rollers, with two lower support rollers and a centrally applied upper loading roller. The support rollers were free to rotate and adjust position slightly during loading, minimising frictional resistance and ensuring appropriate boundary conditions. The loading configuration was symmetric about the notch plane. Dimensions used for the experiments can be found in Table 1.

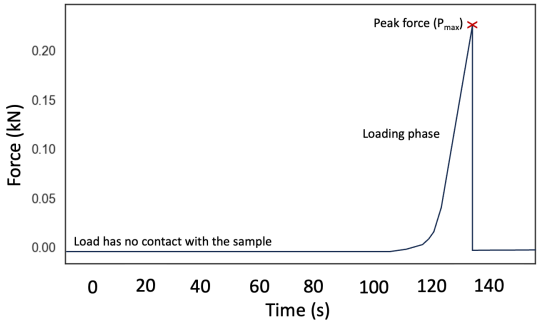


**Figure 5.** Loading phase from a three-point bending experiment on an ice sample, where the peak force is used in the calculation of the mode I fracture toughness.

where $Y'$, the non-dimensional stress intensity factor assuming plane-strain conditions, can be calculated as:

$$Y' = -1.297 + 9.516(S/2R) - (0.47 + 16.457(S/2R))\beta + (1.071 + 34.401(S/2R))\beta^2 \quad (2)$$

where $S$ represents the distance between the rollers, $R$ the radius of the sample, and $\beta = a/R$ (as described in Fig. 4 and Table 1).

A Monte Carlo simulation is used to calculate the uncertainty in fracture toughness with the range of measured radius, thickness and crack length, to include a representative error in the values measured, due to the sensitivity of the method to the sample dimensions, with results from all segments shown in Fig. 6.

In segments 22 and 39, for which both "no-melt" and "melt" samples were available, the presence of melt is associated with an increase in mean fracture toughness (Fig. 6a). In segment 22, the average fracture toughness rises from $76.7 \pm 12.2 - 106.5 \pm 24.9\,\mathrm{kPa\,m^{0.5}}$, representing an increase of nearly 39 %. Segment 39 shows a gain from $107.2 \pm 16.1\,\mathrm{kPa\,m^{0.5}} - 130.8\,\mathrm{kPa\,m^{0.5}}$, a 22 % increase. This strengthening occurs irrespective of the increase in grain size associated with melt, which would traditionally lead to a reduction in toughness when larger grains are present. This demonstrates that the reduction in pore space and the associated increase in density due to melt refreezing plays a greater role in controlling fracture toughness than grain size.

By contrast, samples from segment 35 exhibit a slight decrease in mean toughness upon melting, from $112.7 \pm 25.6\,\mathrm{kPa\,m^{0.5}}$ without melt to $108.2 \pm 10.7\,\mathrm{kPa\,m^{0.5}}$ with melt, a 4 % reduction, well within the combined uncertainty of both groups. This non-significant drop may reflect natural variability in the limited melt-exposed subset, but it does not undermine the broader trend of melt-related toughening observed in the other segments.

Within segment 22, the lowest-density segment analysed, melt had a consistent positive effect, where even small melt fractions of $\sim 0.5 - 1$ % increased toughness compared to melt-free samples. By contrast, in the higher-density segments of 35 and 39, the effect of melt was muted, with toughness values of melt-bearing and melt-free samples overlapping.

Fracture toughness in our dataset shows an expected strong baseline dependence on density, where fracture toughness increases systematically in segments 22, 35 and 39 (Fig. 6b), showing that in these experiments, a key control on fracture toughness is the reduction in porosity and increase in density. This is further supported by how the melt infiltration and refreezing consolidate the firn: in segment 22 density rises from $654.4 \pm 17.2 - 708.7 \pm 76.9\,\mathrm{kg\,m^{-3}}$, in segment 35 from $734.2 \pm 16.1 - 749.2 \pm 46.1\,\mathrm{kg\,m^{-3}}$, and in segment 39 from $716.9 \pm 47.7 - 786.6\,\mathrm{kg\,m^{-3}}$.

Segment 44 departs from this pattern, where despite having the highest mean density of all segments ($824.1 \pm 29.4\,\mathrm{kg\,m^{-3}}$), its fracture toughness remains comparatively low ($98.7 \pm 11.9\,\mathrm{kPa\,m^{0.5}}$). When compared against brine-free segments of the same density, segment 44 samples are systematically weaker by 14 %–34 %, ($20 - 40\,\mathrm{kPa\,m^{0.5}}$). We interpret this discrepancy as a consequence of the brine saturation within the samples. With an average salinity of 2.2 ‰, liquid brine in the pore spaces reduces the intergrain strength, lowers the freezing temperature, and therefore undermines the toughening normally imparted by densification. This

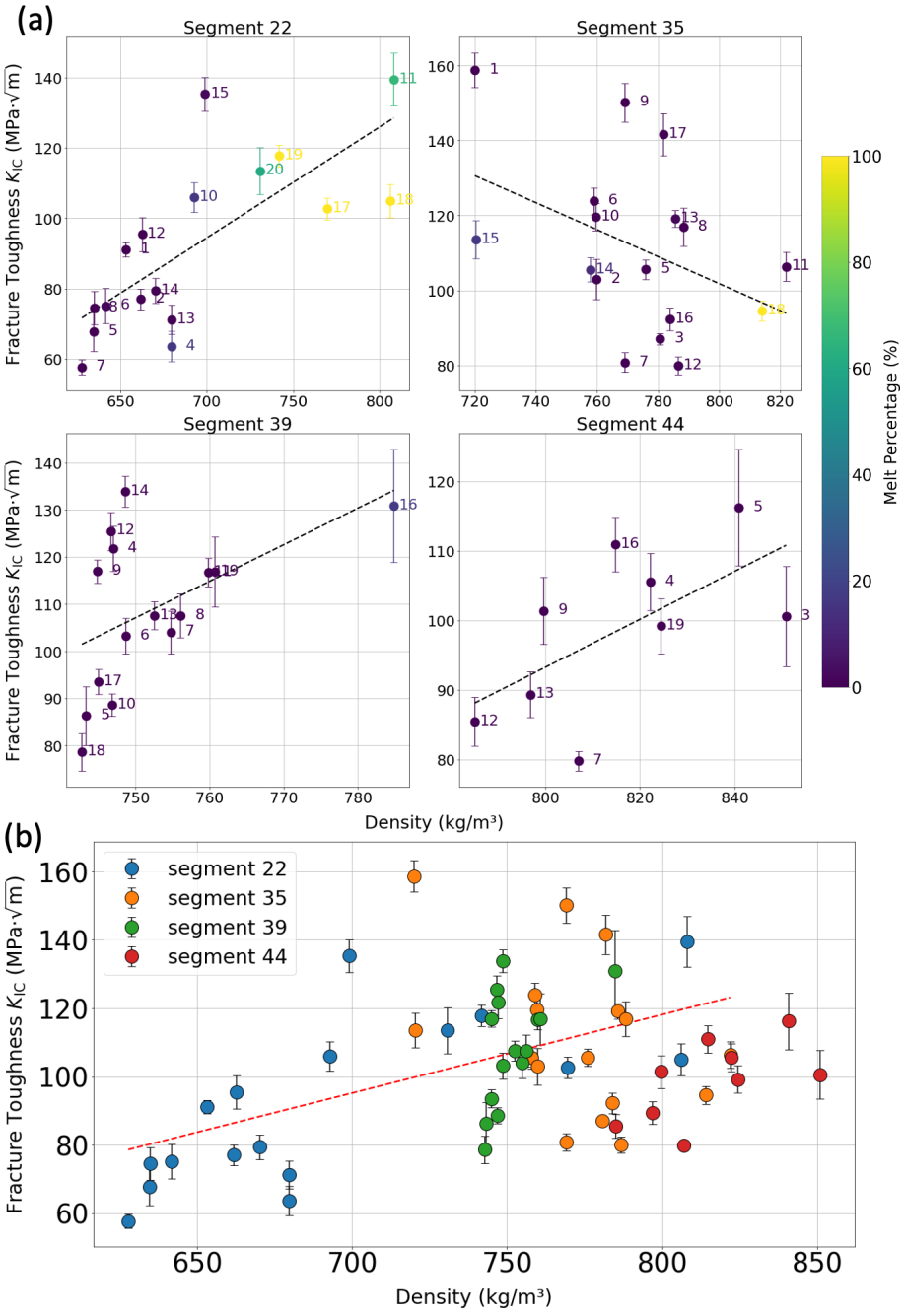


**Figure 6.** **(a)** Fracture toughness measurements from individual segments versus density. Colour indicates the percentage of melt on the fracture surface, where grey indicates no melt, and yellow 100 % melt. **(b)** All fracture toughness values from all four segments versus density, where colour indicates the segment.

weakening is consistent with a decrease in sea ice strength with an increase in brine volume (Weeks, 2010) and with observations of environmentally assisted crack growth in other brittle materials (Atkinson, 1984).

## 5 Discussion

Our experiments demonstrate that fracture toughness in ice shelves varies spatially and with depth. We identify two key processes that are responsible for some of this variability: the inclusion of melt layers and brine saturation. Refrozen melt consistently raises $K_{Ic}$ in meteoric ice (by up to $\sim 40\,\%$), with a greater impact in the shallow firn, whereas brine

infiltration reduces $K_{Ic}$ by 14 %–34 % relative to density-matched, brine-free meteoric ice at the same temperature. Refrozen melt is common on ice shelves, and will become more prevalent in the future, as climate projections indicate greater melt potential and more extreme events (Orr et al., 2023; Kittel et al., 2021; Noël et al., 2023). Brine infiltration occurs when firn at the water line is below sea level, which may also become more common due to ice shelf thinning. Our results demonstrate that as $K_{Ic}$ varies strongly with density, salinity and depth, a spatially and temporally constant toughness value in ice shelf calving models is unlikely to accurately reproduce patterns and timing of ice shelf calving, as theory already shows that including realistic variable, vertical properties can alter predicted crevasse penetration depths by a factor of two (Clayton et al., 2024). A practical way to represent spatially variable $K_{Ic}$ in the case of the BIS would be to use a binary model, assigning one $K_{Ic}$ value to unaltered meteoric ice and a lower $K_{Ic}$ value to brine-saturated infilled ice, where the extent of the brine-saturated unit could be defined from GPR observations.

Our results are consistent with the observation that rifts on the Brunt Ice Shelf accelerate upon reaching zones of brine-saturated infilled ice (lower fracture toughness), with fracture pathways that don't follow the preferential stress direction. Other differences in properties may also play a role, including spatial variations in temperature profile, density profile and overall thickness. It is not possible to assess the ice-shelf wide impact of melt layering, as melt layers are more difficult to quantify spatially and to correlate with crack location. The thickness of the Brunt Ice Shelf makes it relatively sensitive to changes in the firn, and it has already demonstrated its sensitivity to structural changes and external forcing (Marsh et al., 2024, 2025). These laboratory-derived thresholds complement the recent finding that tidal flexure can act as a trigger for rift growth and calving on the Brunt, highlighting how external stresses interact with internal heterogeneity: tides and hydrostatic stresses provide the loading, while melt and brine determine the resistance. Additionally, the BIS temperature profile, with values of around −16 °C at the surface warming to −10 °C at 37 m depth, sits close to the regime where fracture toughness decreases rapidly toward the melting point. These relatively warm conditions at the brine layer would enhance the weakening effect of the brine. However, warmer, softer ice may also relax stresses near a crack tip and reduce the stress intensity driving rift growth (Hulbe et al., 2010). Thus, as accelerated flow enhances ice shelf thinning on the BIS, the balance between refrozen melt strengthening and brine-driven weakening will increasingly dictate how rifts evolve.

Beyond the Brunt, many other Antarctic ice shelves are undergoing rapid change as a consequence of enhanced basal melt, leading to ice shelf thinning and a larger influence of brine-saturated ice. The Amundsen Sea sector is a strong example, where ice shelves have thinned substantially due to ocean-driven melting (Gudmundsson et al., 2019; Pritchard et al., 2012; Reed et al., 2024). Along this coastline, incursions of warm modified Circumpolar Deep Water into ice shelf cavities drives some of the highest basal melt rates observed in Antarctica, averaging 14–27 m $yr^{-1}$ (Jacobs et al., 1992; Dutrieux et al., 2014; Adusumilli et al., 2020; Reed et al., 2024). As a result, ice shelves in this sector (e.g. those from Pine Island, Dutrieux et al., 2014 and Thwaites, Miles et al., 2020) have thinned by tens to hundreds of metres over the past three decades. As thickness declines, the relative influence of the firn and brine horizons in dictating the fracture resistance increases (Cook et al., 2018). As basal thinning enhances the potential for brine infiltration to extend higher into still-permeable firn, as documented on the Brunt and McMurdo ice shelves, this will create weak horizons along which rifts can propagate at accelerated rates (King et al., 2018; Grima et al., 2016).

Our results show that near-surface melt and refreezing processes can alter $K_{Ic}$ by tens of kPa $m^{0.5}$, and that the fracture toughness of firn is not solely governed by grain size or depth, but is strongly modulated by the presence and state of melt. In the shallowest samples (e.g., segment 22), we observe that refrozen melt leads to a substantial increase in fracture toughness (up to 40 % higher than adjacent firn without melt inclusions). This effect appears to stem from localised densification as meltwater fills and refreezes within the pore space, counteracting the expected weakening from larger grain sizes. This interpretation is consistent with field observations from Pine Island Glacier where crevasses were triggered during drilling through an exceptional firn melt layer, implying the layer acted as a mechanically strong unit that had been providing local structural support (Scott et al., 2010). However, this strengthening effect diminishes in denser firn at depth, where the additional density from melt becomes proportionally smaller.

Ice shelves such as Larsen C already contain refrozen melt slabs tens of metres thick (Hubbard et al., 2016), which locally increase $K_{Ic}$ but remove firn air content, reducing the capacity of the firn to buffer future melt and promoting ponding. Although the Brunt Ice Shelf has a unique structural makeup, the material response we observe should apply to other ice shelves where these processes occur. The shelf-wide impact will, however, depend on how extensively melt layers and/or brine horizons are developed and how they are distributed within suture zones. Therefore, for Larsen C, the effect of melt has two possible outcomes. Firstly, such ponding preconditions ice shelves for hydrofracture, the mechanism implicated in the disintegration of Larsen A and B (Scambos et al., 2004). Secondly, melt-induced slab formation may act to temporarily strengthen the ice and alter how rifts propagate by increasing near-surface fracture toughness.

Together, our findings suggest that future ice shelves will comprise a combination of melt-strengthened and brine-weakened ice, with neighbouring units differing in fracture toughness by at least a factor of two. These opposing processes exert controls on rift propagation, meaning that rift

trajectories can be controlled by both local material heterogeneity and large-scale stress fields. By providing the first direct measurements of how melt and brine modify $K_{Ic}$, our study highlights the need for models to incorporate this variability when projecting rift initiation, propagation, and possible ice shelf collapse. Importantly, these results show that ice shelf fracture is not only controlled by geometry and external stresses but also by climate-driven processes that operate in the upper tens of metres of the firn. Future modelling efforts will need to account for the competing influences of refrozen melt and brine infiltration to accurately capture calving thresholds.

## 6 Conclusions

This study provides the first direct measurements of how refrozen surface melt and brine infiltration modify the fracture toughness of meteoric ice from the Brunt Ice Shelf. Laboratory tests show that refrozen melt layers systematically increase $K_{Ic}$ by reducing porosity and increasing density in the firn, with toughness gains of up to approximately 40 %. In contrast, brine infiltration reduces $K_{Ic}$ by 14 %–34 % relative to density-matched meteoric ice, reflecting chemical weakening at grain boundaries and lowered freezing temperatures. Together, these results demonstrate that fracture toughness in ice shelves is neither spatially nor vertically consistent, but varies strongly with density, chemistry and porosity. More broadly, our results highlight how the future stability of the Brunt Ice Shelf, and of Antarctic ice shelves in general, will be governed not just by geometry and stress regime, but by the fine-scale, climate-driven heterogeneity of their structure. Our findings demonstrate that refrozen melt and brine infiltration can shift $K_{Ic}$ by tens of $\mathrm{kPa\,m^{0.5}}$ in opposite directions, even within adjacent ice units. This highlights the importance of incorporating vertical and horizontal variability in toughness into rift and calving models, so that forecasts of ice shelf response to future warming can better capture the competing influences of melt strengthening and brine weakening.

*Code availability.* The analysis in this study was carried out using custom Python scripts developed for data processing and figure generation. These scripts were created specifically for this study and are not maintained as a reusable resource.

*Data availability.* Ice core logs, temperature profiles and the resulting fracture toughness measurements are accessible from the British Antarctic Survey's Polar Data Centre (https://doi.org/10.5285/c059bb26-276d-4be6-ae8c-778aee12a3b4, Pearce et al., 2026).

*Author contributions.* EP and ERT collected the ice cores in the 2023/2024 Antarctic season. EP, TMM, and JT performed the ice fracture experiments and fracture toughness calculations. OJM acquired the project funding. SJ produced the salinity measurements. EP wrote the manuscript, and OJM, TMM, JT and SJ contributed to edits and revisions.

*Competing interests.* The contact author has declared that none of the authors has any competing interests.

*Disclaimer.* Publisher's note: Copernicus Publications remains neutral with regard to jurisdictional claims made in the text, published maps, institutional affiliations, or any other geographical representation in this paper. The authors bear the ultimate responsibility for providing appropriate place names. Views expressed in the text are those of the authors and do not necessarily reflect the views of the publisher.

*Acknowledgements.* This research was supported by the Natural Environment Research Council (NERC, grant number NE/X014991/1). Fieldwork and ice core collection was made possible by the dedicated efforts of the British Antarctic Survey's Halley VI operations team and drill engineers during the 2023/2024 season. We thank Shaun Miller for assistance with ice preparation and line scanning. Jukka Tuhkuri was supported by the Research Council of Finland (decision number 351229). Siobhan Johnson receives funding from the Yusuf Hamied Foundation, provided through the Yusuf Hamied Department of Chemistry. We also acknowledge the use of OpenAI (https://chat.openai.com, last access: 3 October 2025) for assistance with Python code development and manuscript editing.

*Financial support.* This research has been supported by the Natural Environment Research Council (grant no. NE/X014991/1).

*Review statement.* This paper was edited by Christian Haas and reviewed by Lisa Craw and one anonymous referee.

## References

Adusumilli, S., Fricker, H. A., Medley, B., Padman, L., and Siegfried, M. R.: Interannual variations in meltwater input to the Southern Ocean from Antarctic ice shelves, Nat. Geosci., 13, 616–620, 2020.

Albrecht, T. and Levermann, A.: Fracture field for large-scale ice dynamics, J. Glaciol., 58, 165–176, 2012.

Alley, R. B. and Bentley, C. R.: Ice-core analysis on the Siple Coast of West Antarctica, Ann. Glaciol., 11, 1–7, 1988.

Atkinson, B. K.: Subcritical crack growth in geological materials, J. Geophys. Res.-Sol. Ea., 89, 4077–4114, 1984.

Bassis, J., Coleman, R., Fricker, H., and Minster, J.: Episodic propagation of a rift on the Amery Ice Shelf, East Antarctica, Geophys.

Res. Lett., 32, L06502, https://doi.org/10.1029/2004GL022048, 2005.

Borstad, C., Khazendar, A., Larour, E., Morlighem, M., Rignot, E., Schodlok, M., and Seroussi, H.: A damage mechanics assessment of the Larsen B ice shelf prior to collapse: Toward a physically-based calving law, Geophys. Res. Lett., 39, L18502, https://doi.org/10.1029/2012GL053317, 2012.

Borstad, C., McGrath, D., and Pope, A.: Fracture propagation and stability of ice shelves governed by ice shelf heterogeneity, Geophys. Res. Lett., 44, 4186–4194, 2017.

Christmann, J., Müller, R., Webber, K. G., Isaia, D., Schader, F. H., Kipfstuhl, S., Freitag, J., and Humbert, A.: Measurement of the fracture toughness of polycrystalline bubbly ice from an Antarctic ice core, Earth Syst. Sci. Data, 7, 87–92, https://doi.org/10.5194/essd-7-87-2015, 2015.

Clayton, T., Duddu, R., Hageman, T., and Martínez-Pañeda, E.: The influence of firn layer material properties on surface crevasse propagation in glaciers and ice shelves, The Cryosphere, 18, 5573–5593, https://doi.org/10.5194/tc-18-5573-2024, 2024.

Cook, S., Galton-Fenzi, B. K., Ligtenberg, S. R. M., and Coleman, R.: Brief communication: widespread potential for seawater infiltration on Antarctic ice shelves, The Cryosphere, 12, 3853–3859, https://doi.org/10.5194/tc-12-3853-2018, 2018.

Craw, L., McCormack, F. S., Cook, S., Roberts, J., and Treverrow, A.: Modelling the influence of marine ice on the dynamics of an idealised ice shelf, J. Glaciol., 69, 342–352, 2023.

Cruz, C. and Lipovsky, B. P.: Fracturing during freezing in salty ice: preliminary analysis using a low-cost model system, Earth ArXiv [preprint], https://doi.org/10.31223/X5P994, 2025.

Cullen, D. and Baker, I.: Observation of impurities in ice, Microsc. Res. Techniq., 55, 198–207, 2001.

De Rydt, J., Gudmundsson, G. H., Nagler, T., and Wuite, J.: Calving cycle of the Brunt Ice Shelf, Antarctica, driven by changes in ice shelf geometry, The Cryosphere, 13, 2771–2787, https://doi.org/10.5194/tc-13-2771-2019, 2019.

Dempsey, J. P.: The fracture toughness of ice, in: Ice-Structure Interaction: IUTAM/IAHR Symposium St. John's, Newfoundland Canada 1989, 109–145, Springer, 109–145, https://doi.org/10.1007/978-3-642-84100-2, ISBN 978-3-642-84100-2, 1991.

Dutrieux, P., De Rydt, J., Jenkins, A., Holland, P. R., Ha, H. K., Lee, S. H., Steig, E. J., Ding, Q., Abrahamsen, E. P., and Schröder, M.: Strong sensitivity of Pine Island ice-shelf melting to climatic variability, Science, 343, 174–178, 2014.

Foster, T. D. and Carmack, E. C.: Temperature and salinity structure in the Weddell Sea, J. Phys. Oceanogr., 6, 36–44, 1976.

Fricker, H., Bassis, J., Minster, B., and MacAyeal, D.: ICESat's new perspective on ice shelf rifts: The vertical dimension, Geophys. Res. Lett., 32, L23S08, https://doi.org/10.1029/2005GL025070, 2005a.

Fricker, H., Young, N., Coleman, R., Bassis, J., and Minster, J.-B.: Multi-year monitoring of rift propagation on the Amery Ice Shelf, East Antarctica, Geophys. Res. Lett., 32, L02502, https://doi.org/10.1029/2004GL021036, 2005b.

Glasser, N. and Scambos, T. A.: A structural glaciological analysis of the 2002 Larsen B ice-shelf collapse, J. Glaciol., 54, 3–16, 2008.

Grima, C., Greenbaum, J. S., Lopez Garcia, E. J., Soderlund, K. M., Rosales, A., Blankenship, D. D., and Young, D. A.: Radar detection of the brine extent at McMurdo Ice Shelf, Antarctica, and its control by snow accumulation, Geophys. Res. Lett., 43, 7011–7018, 2016.

Gudmundsson, G. H., Paolo, F. S., Adusumilli, S., and Fricker, H. A.: Instantaneous Antarctic ice sheet mass loss driven by thinning ice shelves, Geophys. Res. Lett., 46, 13903–13909, 2019.

Hubbard, B., Luckman, A., Bevan, S., Ashmore, D. W., Kulessa, B., Kuipers Munneke, P., Philippe, M., Jansen, D., Booth, A., Sevestre, H., Tison, J.-L., O'Leary, M., and Rutt, I.: Massive subsurface ice formed by refreezing of ice-shelf melt ponds, Nat. Commun., 7, 11897, https://doi.org/10.1038/ncomms11897, 2016.

Hulbe, C. L., LeDOUX, C., and Cruikshank, K.: Propagation of long fractures in the Ronne Ice Shelf, Antarctica, investigated using a numerical model of fracture propagation, J. Glaciol., 56, 459–472, 2010.

Huth, A., Duddu, R., Smith, B., and Sergienko, O.: Simulating the processes controlling ice-shelf rift paths using damage mechanics, J. Glaciol., 69, 1915–1928, 2023.

Jacobs, S. S., Helmer, H., Doake, C. S., Jenkins, A., and Frolich, R. M.: Melting of ice shelves and the mass balance of Antarctica, J. Glaciol., 38, 375–387, 1992.

Killingbeck, S. F., Kulessa, B., Miles, K. E., Hubbard, B., Luckman, A., Thompson, S. S., Jones, G., and Galton-Fenzi, B. K.: Imaging brine infiltration and basal marine ice in Larsen C Ice Shelf, Antarctic Peninsula, from borehole measurements and transient electromagnetics, Geophys. Res. Lett., 52, e2025GL115908, https://doi.org/10.1029/2025GL115908, 2025.

King, E. C., De Rydt, J., and Gudmundsson, G. H.: The internal structure of the Brunt Ice Shelf from ice-penetrating radar analysis and implications for ice shelf fracture, The Cryosphere, 12, 3361–3372, https://doi.org/10.5194/tc-12-3361-2018, 2018.

Kittel, C., Amory, C., Agosta, C., Jourdain, N. C., Hofer, S., Delhasse, A., Doutreloup, S., Huot, P.-V., Lang, C., Fichefet, T., and Fettweis, X.: Diverging future surface mass balance between the Antarctic ice shelves and grounded ice sheet, The Cryosphere, 15, 1215–1236, https://doi.org/10.5194/tc-15-1215-2021, 2021.

Krug, J., Weiss, J., Gagliardini, O., and Durand, G.: Combining damage and fracture mechanics to model calving, The Cryosphere, 8, 2101–2117, https://doi.org/10.5194/tc-8-2101-2014, 2014.

Kulessa, B., Booth, A. D., O'Leary, M., McGrath, D., King, E. C., Luckman, A. J., Holland, P. R., Jansen, D., Bevan, S. L., Thompson, S. S., and Hubbard, B.: Seawater softening of suture zones inhibits fracture propagation in Antarctic ice shelves, Nat. Commun., 10, 5491, https://doi.org/10.1038/s41467-019-13539-x, 2019.

Kuruppu, M. D., Obara, Y., Ayatollahi, M. R., Chong, K., and Funatsu, T.: ISRM-suggested method for determining the mode I static fracture toughness using semi-circular bend specimen, Rock Mech. Rock Eng., 47, 267–274, 2014.

Larour, E., Rignot, E., and Aubry, D.: Modelling of rift propagation on Ronne Ice Shelf, Antarctica, and sensitivity to climate change, Geophys. Res. Lett., 31, L16404, https://doi.org/10.1029/2004GL020077, 2004.

Lewis, E.: The practical salinity scale 1978 and its antecedents, IEEE J. Oceanic Eng., 5, 3–8, 1980.

Lipovsky, B. P.: Ice shelf rift propagation and the mechanics of wave-induced fracture, J. Geophys. Res.-Oceans, 123, 4014–4033, 2018.

Lipovsky, B. P.: Ice shelf rift propagation: stability, three-dimensional effects, and the role of marginal weakening, The Cryosphere, 14, 1673–1683, https://doi.org/10.5194/tc-14-1673-2020, 2020.

Marsh, O., Arthern, R., and De Rydt, J.: Ocean tides trigger ice shelf rift growth and calving, Nat. Commun., 16, 6697, https://doi.org/10.1038/s41467-025-61796-w, 2025.

Marsh, O. J., Luckman, A. J., and Hodgson, D. A.: Brief communication: Rapid acceleration of the Brunt Ice Shelf after calving of iceberg A-81, The Cryosphere, 18, 705–710, https://doi.org/10.5194/tc-18-705-2024, 2024.

Miles, B., Stokes, C., Jenkins, A., Jordan, J., Jamieson, S., and Gudmundsson, G.: Intermittent structural weakening and acceleration of the Thwaites Glacier Tongue between 2000 and 2018, J. Glaciol., 66, 485–495, 2020.

Mulvaney, R., Bremner, S., Tait, A., and Audley, N.: A medium-depth ice core drill, Memoirs of National Institute of Polar Research, 56, 82–90, 2002.

Naughten, K. A., Holland, P. R., and De Rydt, J.: Unavoidable future increase in West Antarctic ice-shelf melting over the twenty-first century, Nat. Clim. Change, 13, 1222–1228, 2023.

Nicola, L., Notz, D., and Winkelmann, R.: Revisiting temperature sensitivity: how does Antarctic precipitation change with temperature?, The Cryosphere, 17, 2563–2583, https://doi.org/10.5194/tc-17-2563-2023, 2023.

Nixon, W. and Schulson, E.: A micromechanical view of the fracture toughness of ice, Le Journal de Physique Colloques, 48, C1-313–C1-319, https://doi.org/10.1051/jphyscol:1987144, 1987.

Noël, B., Van Wessem, J. M., Wouters, B., Trusel, L., Lhermitte, S., and Van Den Broeke, M. R.: Higher Antarctic ice sheet accumulation and surface melt rates revealed at 2 km resolution, Nat. Commun., 14, 7949, https://doi.org/10.1038/s41467-023-43584-6, 2023.

Orr, A., Deb, P., Clem, K. R., Gilbert, E., Bromwich, D. H., Boberg, F., Colwell, S., Hansen, N., Lazzara, M. A., Mooney, P. A., Mottram, R. H., Niwano, M., Phillips, T., Pishniak, D., Reijmer, C. H., van de Berg, W. J., Webster, S., and Zou, X.: Characteristics of surface "melt potential" over Antarctic ice shelves based on regional atmospheric model simulations of summer air temperature extremes from 1979/80 to 2018/19, J. Climate, 36, 3357–3383, 2023.

Pearce, E., Marsh, O., and Thomas, E.: Ice core physical property data from Brunt Ice Shelf close to the site of Halley VI Research Station from 2023/2024 and 2024/2025 (Version 1.0), NERC EDS UK Polar Data Centre [data set], https://doi.org/10.5285/c059bb26-276d-4be6-ae8c-778aee12a3b4, 2026.

Pralong, A. and Funk, M.: Dynamic damage model of crevasse opening and application to glacier calving, J. Geophys. Res.-Sol. Ea., 110, B01309, https://doi.org/10.1029/2004JB003104, 2005.

Pritchard, H., Ligtenberg, S. R., Fricker, H. A., Vaughan, D. G., van den Broeke, M. R., and Padman, L.: Antarctic ice-sheet loss driven by basal melting of ice shelves, Nature, 484, 502–505, 2012.

Reed, B., Green, J. A. M., Jenkins, A., and Gudmundsson, G. H.: Melt sensitivity of irreversible retreat of Pine Island Glacier, The Cryosphere, 18, 4567–4587, https://doi.org/10.5194/tc-18-4567-2024, 2024.

Rist, M., Sammonds, P., Murrell, S., Meredith, P., Oerter, H., and Doake, C.: Experimental fracture and mechanical properties of Antarctic ice: preliminary results, Ann. Glaciol., 23, 284–292, 1996.

Rist, M., Sammonds, P., Oerter, H., and Doake, C.: Fracture of Antarctic shelf ice, J. Geophys. Res.-Sol. Ea., 107, ECV 2-1–ECV 2-13, https://doi.org/10.1029/2000JB000058, 2002.

Scambos, T., Fricker, H. A., Liu, C.-C., Bohlander, J., Fastook, J., Sargent, A., Massom, R., and Wu, A.-M.: Ice shelf disintegration by plate bending and hydro-fracture: Satellite observations and model results of the 2008 Wilkins ice shelf break-ups, Earth Planet. Sc. Lett., 280, 51–60, 2009.

Scambos, T. A., Bohlander, J., Shuman, C. A., and Skvarca, P.: Glacier acceleration and thinning after ice shelf collapse in the Larsen B embayment, Antarctica, Geophys. Res. Lett., 31, L18402, https://doi.org/10.1029/2004GL020670, 2004.

Schulson, E. M.: Brittle failure of ice, Eng. Fract. Mech., 68, 1839–1887, 2001.

Schulson, E. M. and Duval, P.: Creep and fracture of ice, Cambridge University Press, ISBN 978-0521806206, 2009.

Scott, J. B., Smith, A. M., Bingham, R. G., and Vaughan, D. G.: Crevasses triggered on Pine Island Glacier, West Antarctica, by drilling through an exceptional melt layer, Ann. Glaciol., 51, 65–70, 2010.

Timco, G. W. and Frederking, R. M. W.: Flexural strength and fracture toughness of sea ice, Cold Reg. Sci. Technol., 8, 35–41, 1983.

Van der Veen, C.: Fracture mechanics approach to penetration of surface crevasses on glaciers, Cold Reg. Sci. Technol., 27, 31–47, 1998.

van der Veen, C. J.: Fracture mechanics approach to penetration of bottom crevasses on glaciers, Cold Reg. Sci. Technol., 27, 213–223, https://doi.org/10.1016/S0165-232X(98)00006-8, 1998.

Walker, C., Bassis, J., Fricker, H., and Czerwinski, R.: Structural and environmental controls on Antarctic ice shelf rift propagation inferred from satellite monitoring, J. Geophys. Res.-Earth, 118, 2354–2364, 2013.

Weeks, W.: On sea ice, University of Alaska Press, ISBN 978-1-60223-079-8, 2010.

Weiss, J.: Subcritical crack propagation as a mechanism of crevasse formation and iceberg calving, J. Glaciol., 50, 109–115, 2004.

Wille, J. D., Favier, V., Jourdain, N. C., Kittel, C., Turton, J. V., Agosta, C., Gorodetskaya, I. V., Picard, G., Codron, F., Leroy-Dos Santos, C., Amory, C., Fettweis, X., Blanchet, J., and Berchet, A.: Intense atmospheric rivers can weaken ice shelf stability at the Antarctic Peninsula, Communications Earth and Environment, 3, 90, https://doi.org/10.1038/s43247-022-00422-9, 2022.